Empirical Estimate of Forestation-Induced Precipitation Changes in Europe

Journal Article

Author(s):
Meier, Ronny; Schwaab, Jonas; Seneviratne, Sonia I.; Sprenger, Michael; Lewis, Elizabeth; Davin, Edouard Léopold

Publication date:
2021-07

Permanent link:
https://doi.org/10.3929/ethz-b-000493339

Originally published in:
Nature Geoscience 14, https://doi.org/10.1038/s41561-021-00773-6

Funding acknowledgement:
172715 - CLimate IMPacts of Utilizing Land in Switzerland and Europe (CLIMPULSE) (SNF)

Supplementary Material of "Empirical Estimate of Forestation-Induced Precipitation Changes in Europe"

https://doi.org/10.1038/s41561-021-00773-6

Ronny Meier[1,*], Jonas Schwaab[1], Sonia I. Seneviratne[1], Michael Sprenger[1], Elizabeth Lewis[2], and Edouard L. Davin[1,*]

[1]ETH Zurich, Institute for Atmospheric and Climate Science, Universitaetstrasse 16, 8092 Zurich, Switzerland
[2]Newcastle University, School of Engineering, Newcastle upon Tyne, NE1 7RU, United Kingdom
[*]Correspondance to: ronny.meier@env.ethz.ch or edouard.davin@env.ethz.ch

Contents

A Sensitivity of downwind precipitation changes to location of forestation

As for the local effect, the location of forestation is important for downwind alterations of precipitation. Here, we briefly discuss the downwind change in precipitation due to forestation (ΔP_{dw}) from two additional forestation scenarios besides the European-wide 20 % forestation: (1) foresting 20 % of the land in areas with an annual mean upwind coast distance (Extended Data Fig. 2 d) less than 5° and (2) foresting 20 % of the land in areas with an annual mean upwind coast distance exceeding 5° (corresponding to 557 km). This is done by recalculating the upwind land cover (LC) fractions as described in 'Estimating the theoretical effect of forestation on precipitation' in the Methods, if forestation only occurs in the respective regions of interest.

Forestation over areas with an average upwind coast distance of less than 5° explains most of the estimated ΔP_{dw} in winter, while forestation over areas further away from the coast has only a minor downwind effect on precipitation (Fig. A1 a, d, g, and j). In summer on the other hand, forestation over the more continental regions of Europe increases precipitation over those areas, indicating that the high evapotranspiration of forests can be an important source of moisture in continental climates (Fig. A1 b, e, h, and k). This is consistent with the finding that atmospheric moisture recycling in the northern mid-latitudes is unimportant during winter but substantial during summer[1] (also see Supplement C). It therefore appears that the downwind reduction in winter precipitation due to forestation can be avoided by prohibiting forestation in areas close to the coast, while still profiting from the downwind increase in precipitation during summer. It needs to be mentioned however that forestation over the continental parts of Europe might affect winter precipitation in regions that lie outside of our study domain.

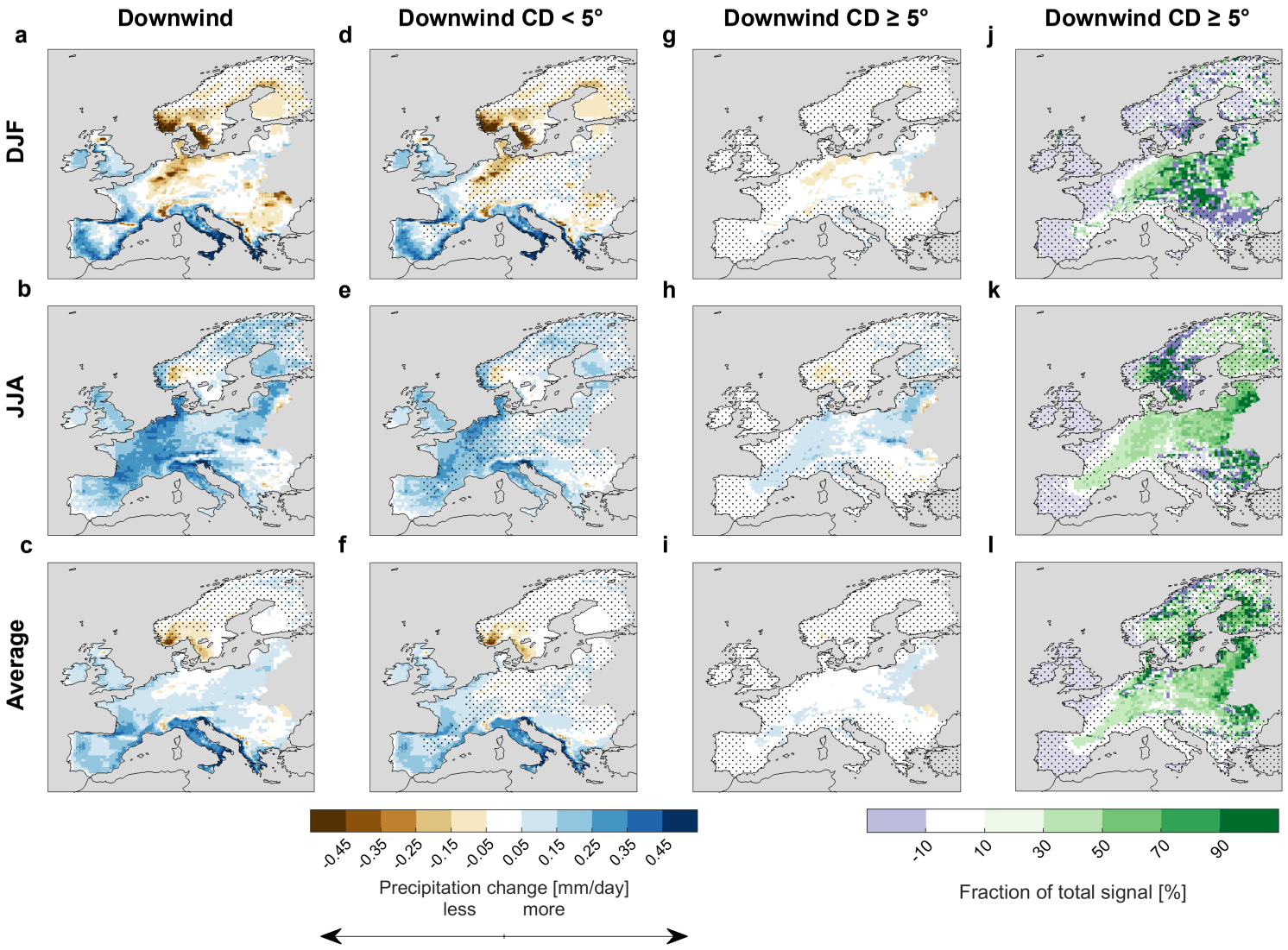

Figure A1. Estimated downwind precipitation change (a-c) after foresting 20 % of the land surface in the entire study domain (Fig. 2 d-f repeated for convenience). To the right, downwind precipitation change from foresting 20 % of the land surface over areas with an annual mean upwind coast distance smaller than 5°(d-f) and larger than 5°(g-i). Stippling depicts areas that were not forested in the respective scenario. On the very right, fraction of panels a-c explained by panels g-i. Top row boreal winter (DJF), middle row boreal summer (JJA), and bottom row annual mean.

B The role of surface roughness

It was hypothesized in the main part of this study that the higher surface roughness of forests compared to rainfed agricultural land (AL_r) is an important physical driver of the estimated precipitation changes from forestation through altering the propagation speed of precipitating air masses and inducing turbulence. Here, we analyze the connection of the monthly ERA5-Land[2] wind speed 10 m above the surface (WS) and the propagation speed of the wind trajectories (PS), calculated from the upwind coast distance divided by the upwind coast time (see 'Trajectory-based fields' in the Methods), to forestation and precipitation. We use these two variables as a proxy for the local surface roughness in the case of WS and the upwind surface roughness prior to precipitation events in the case of PS. We present results from three additional generalized additive models (GAMs) in this section: Two GAMs of the same structure as the GAM of the main part (Extended Data Table 1), but with WS and PS as the response variables instead of the MSWEP precipitation climatology. The third GAM is composed of a number of 's' terms for various physical variables that might affect precipitation, including WS and PS (Table B1), and is fitted to the MSWEP precipitation climatology as described in 'GAM construction' in the Methods. With the latter GAM, we estimate the change in precipitation associated with an 1 m/s increase in WS by subtracting a GAM prediction where WS was decreased by 0.5 m/s from a GAM prediction where WS was increased by 0.5 m/s. Using the same procedure, we estimate the change in precipitation following a 4 m/s increase in PS.

During the winter months, the latter GAM identifies a pronounced link between precipitation and wind speed (Fig. B1 a and d). Higher surface wind speeds are associated with lower precipitation, implying that rougher surfaces receive more precipitation. According to the GAM that was fitted to WS, forestation results in a decrease of WS during this season in most regions of the study domain, in particular in Regions 1 and 2, where the local change in precipitation due to forestation (ΔP_{loc}) was highest (Fig. B2 a). Further, a faster propagation of the air masses from the coast to the precipitation event is associated with higher amount of precipitation during winter (Fig. B1 d). Forestation appears to hinder the propagation of precipitation events towards the continental regions of Europe, as indicated by the estimation reduction in downwind PS due to forestation (Fig. B2 d-f). This conforms with the positive ΔP_{dw} along the southern and western coastal regions of Europe and the neutral to negative ΔP_{dw} toward the East (Fig.2). During summer on the other hand, the relationship between precipitation and WS is weaker, in agreement with the less positive ΔP_{loc} than during winter. Also, we find an only minor connection of PS and precipitation, implying that different processes such as evapotranspiration are more relevant for the estimated ΔP_{dw} during this season.

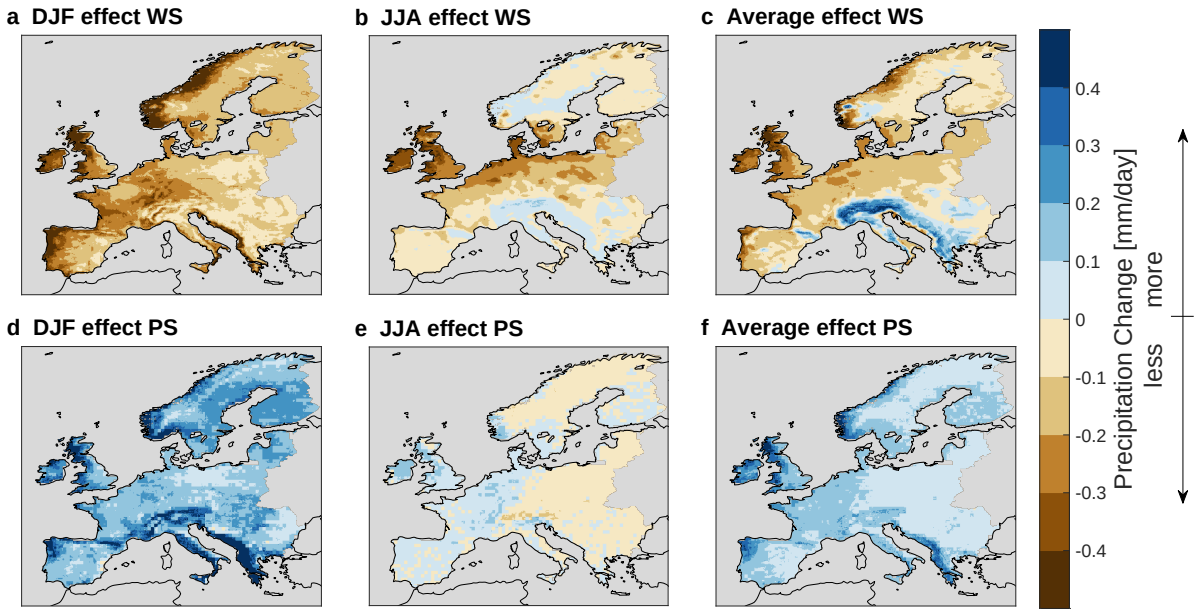

Figure B1. Panels a-c, change in precipitation associated with a WS increase of 1 m/s. Panels d-f, change in precipitation associated with a PS increase of 4 m/s. Left column boreal winter, middle column boreal summer, and right column annual mean.

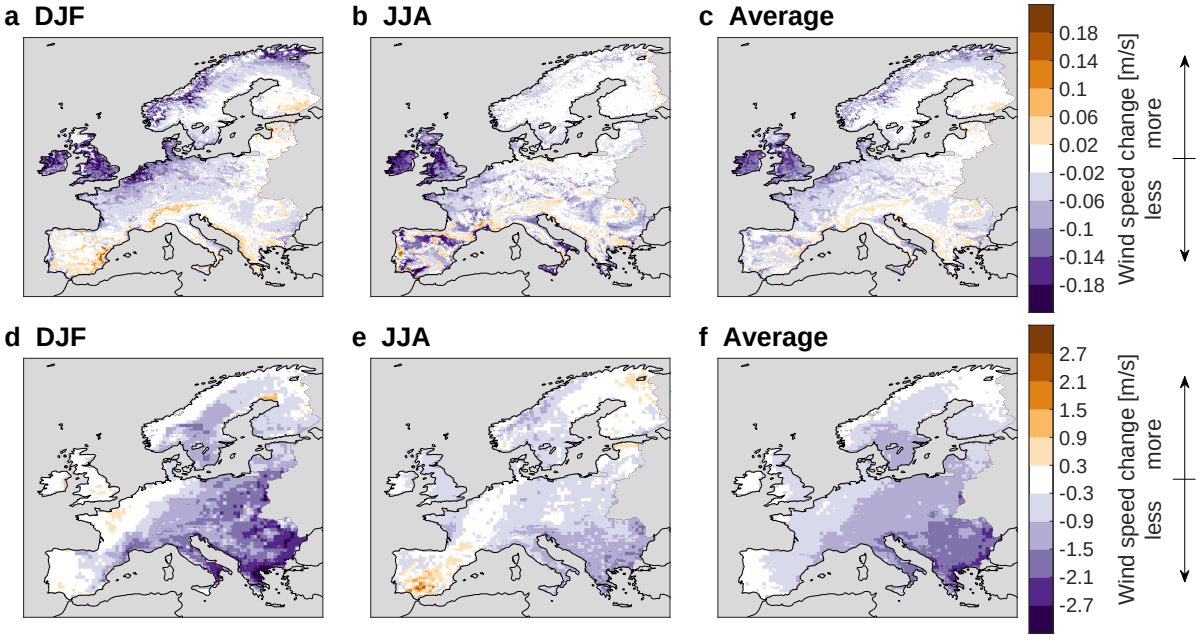

Figure B2. Panels a-c, estimated local change in WS from foresting 20 % of the land surface in the entire study domain. Panels d-f, estimated downwind change in PS from the same forestation scenario. Left column boreal winter, middle column boreal summer, and right column annual mean.

Table B1. Terms used to construct the GAM with potential physical drivers of precipitation. Consult 'GAM construction' in the Methods for more information on meaning of terms and construction of GAM.

Variable(s)	Type	k	sp	Data source
alt	s	10	estimated	EU-DEM v1.1
expo	s	10	estimated	EU-DEM v1.1
slope	s	10	estimated	EU-DEM v1.1
TPI	s	10	estimated	EU-DEM v1.1
TRI	s	10	estimated	EU-DEM v1.1
dw_hd	s	10	estimated	ERA5
uw_cd	s	10	estimated	ERA5
uw_hd	s	10	estimated	ERA5
PS	s	10	estimated	ERA5
Albedo	s	10	estimated	ERA5-Land
Latent heat flux	s	10	estimated	ERA5-Land
Sensible heat flux	s	10	estimated	ERA5-Land
t2m	s	10	estimated	ERA5-Land
ws	s	10	estimated	ERA5-Land
lat, lon	ti	15	5	-

C Moisture source diagnostic

In this supplement we apply the Lagrangian moisture source diagnostic[3] to the air parcel trajectories described in the Methods in order to inspect the importance of the different LC types as a moisture source for precipitation. This diagnostic attributes moisture uptake along a Lagrangian trajectory to a precipitation event at the end of this trajectory by tracking the specific humidity of the air parcel along its path (for a more detailed description check Sodemann et al., 2008[3]). We deviate from the method as described in Sodemann et al. (2008) on three aspects: (1) We apply the diagnostic at hourly instead of 6-hourly temporal resolution. (2) We remove the threshold for the minimal change in specific humidity for a moisture uptake to be identified; i.e, any change in specific humidity is treated. (3) We do not check whether an identified moisture uptake occurred within the planetary boundary layer, as was done in a follow-up study using the same diagnostic[4]. Ultimately, the diagnostic retrieves the fraction of moisture provided from each point the trajectory overpassed to the final precipitation event. We then divide the fraction of the moisture provided by each point into fractions from the different LCs proportionally to the CORINE Land Cover fractions at this point. As a result, it can be quantified for each trajectory, which fraction of the final precipitation event was supplied by each LC class, by summing the fractions contributed by the individual LC types along the trajectory. These fractions are then converted into contributions (in mm/h) by multiplying the fractions with the precipitation rate at the end of the trajectory. Finally, we calculate the median contribution from each LC class for each location and month.

The moisture source diagnostic reveals that the moisture supply for precipitation is fundamentally different between summer and winter. During winter, the vast majority water vapor originates from open water (Fig. C1 a). Along the coasts, both AL_r and forests provide hardly any moisture for precipitation (Fig. C1 c and e), indicating that the downwind precipitation increase due to forestation in those regions (Fig. 2 d and Fig. 3 d) is rather the result of altered atmospheric dynamics than an alteration in moisture supply. On the other hand, reduced downwind precipitation due to forestation in Central Europe and Scandinavia is at least partly explained by reduced moisture supply for precipitation following forestation (Fig. C1 g). During summer, the contribution of open water to precipitation declines sharply moving away from the coast, which exemplifies the importance of moisture supply from land during this season (Fig. C1 b). Both AL_r and forest contribute over-proportionally to precipitation in comparison to the upwind LC fractions associated with these LCs (Fig. C1 d and f). However, this over-proportionality is more pronounced for forest, indicating that increased ET over forests in comparison to AL_r can explain the remote increase in precipitation following forestation that is found in the main part of this study (Fig. 2 e and Fig. 3 e).

While the results from the moisture source diagnostic conform overall with the ΔP_{dw} from the main part of this study, there are some limitations to this analysis. Firstly, the moisture source diagnostic cannot capture mechanisms other than moisture supply, such as slowing down the propagation of precipitating air masses or preferential triggering of convection over a certain LC. This is most obvious in coastal regions during winter, where moisture contributions from AL_r and forest can clearly not explain the remote precipitation increase following forestation in those areas. Secondly, we assume that the moisture uptake at a certain position is originating from the different LC types proportionally to their fractional coverage, which is an oversimplification. Finally, it cannot account for local modifications in precipitation by specific LC types. Given our results of locally increased precipitation over forests in comparison to AL_r, an underestimation of the moisture supply from forests appears likely, as part of their moisture supply is compensated by increased precipitation over forests, which leads to a reduction of the specific humidity.

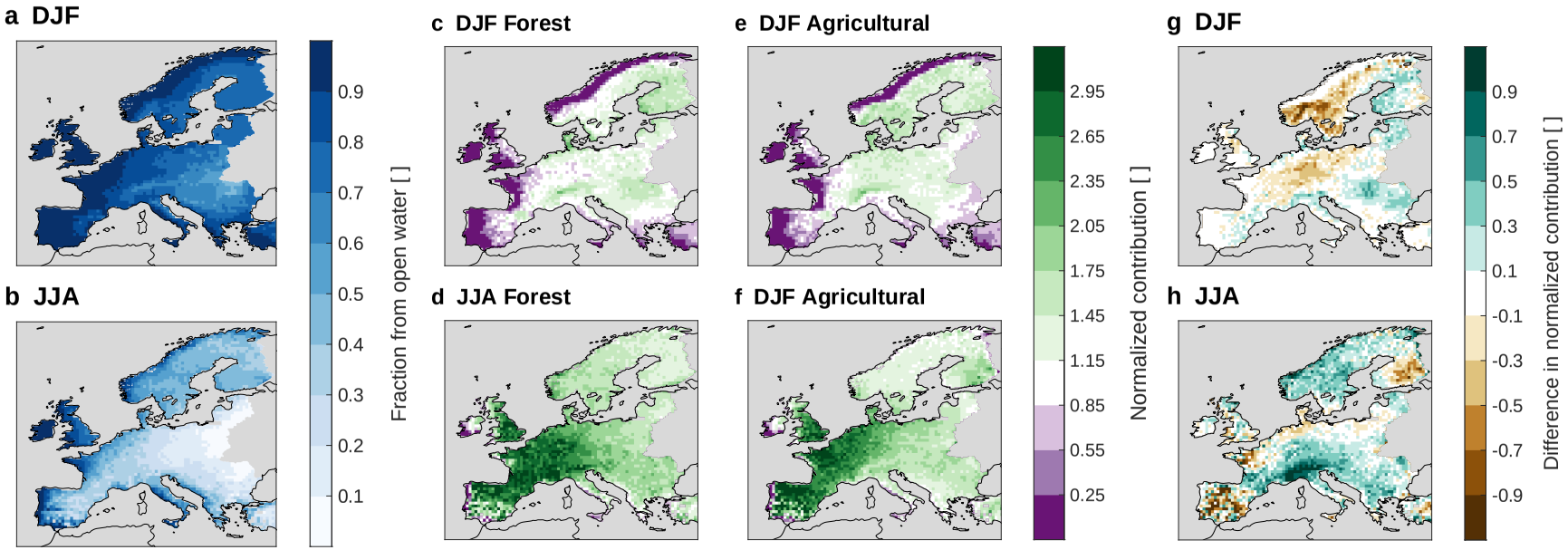

Figure C1. Panels a and b, fraction of precipitation in ERA5 trajectories originating from open water. Panels c-f, fraction of precipitation in ERA5 trajectories originating from forest (c, d) and AL_r (e, f) normalized by the upwind LC fraction of the respective LC. Values above one indicate that the respective LC is contributing over-proportionally to precipitation in comparison to its upwind LC fraction and below one under-proportionally. Panels g and h, difference in normalized contribution between forest (c, d) and AL_r (e, f). Top row boreal winter and bottom row boreal summer.

D Sensitivity of site pair analysis to selection criteria

Here, we present sensitivity tests of the site pair analysis to the selection criteria of the site pairs, which are summarized in Table D1. Overall, the site pair analysis is affected by a trade-off between the necessity of obtaining large enough sample size to reduce the influence of noise and excluding confounding factors by applying stricter selection criteria (Fig. D1 a). With an increasing number of site pairs the agreement between the full GAM and the rain gauges measurements increases. Synchronously however, the fraction of the precipitation difference of the sites with higher forest coverage minus the sites with more rainfed agricultural land (ΔP_{loc}) that can be explained by other factors than land cover increases, resulting in an increasing index of agreement (IA) between the 'no LC' GAM and the rain gauges. The IA of the portion of ΔP_{loc} that is explained by the differences in rainfed agricultural land (AL_r) and forest fraction in the GAM exhibits an optimum at approximately 1000 to 2000 sites.

The magnitude of the median ΔP_{loc} increases with an increasing minimum threshold for the differences in the fractions of AL_r and forest (Fig. D1 b). However, this increasing tendency weakens towards higher minimum thresholds, implying that ΔP_{loc} is nonlinear and saturates for higher rates of forestation. ΔP_{loc} tends to strengthen for higher thresholds also in Region 1, with the exception of the highest threshold, for which the robustness of the signal disintegrates due to the small sample size (Fig. D1 d). ΔP_{loc} also exhibits a weak increasing tendency when relaxing other selection criteria than the fractions of AL_r and forest (Fig. D1 c). This likely originates from the increasing influence of confounding factors for the median ΔP_{loc}, as indicated by the higher IAs for the 'no LC' GAM for larger numbers of site pairs. More distinctively, the spread among the site pairs increases, implying that relaxed selection criteria result in more noise due to other variables than the AL_r and forest fractions.

Table D1. Sensitivity tests for selection criteria. From left to right, identification number of sensitivity test, number of site pairs found in respective test, minimum thresholds for difference in fraction of AL_r and forest, minimum threshold for sum of the AL_r and forest fractions, as well as maximum thresholds for distance between sites, altitude difference, difference in open water fraction, difference in upwind open water fraction, difference in slope, difference in TRI, and difference in annual mean upwind distance to coast. Last column, median annual mean ΔP_{loc} across all site pairs and interquartile range of annual mean ΔP_{loc} in brackets.

ID	N	ΔLC [%]	Sum [%]	Dist. [°]	Alt. [m]	pct_opwa [%]	uw_pct_opwa [%]	Slope [°]	TRI [m]	uw_cd [°]	Median ΔP_{loc} [mm/day]
1	199	30	50	0.50	15	15	15	4	2	0.20	0.14 (0.02-0.27)
2	319	40	50	0.75	25	20	20	5	3	0.25	0.17 (0.07-0.31)
3	645	25	50	0.60	20	15	15	5	3	0.25	0.15 (0.04-0.29)
4	721	30	50	0.75	25	20	20	5	3	0.25	0.17 (0.06-0.31)
5	1112	20	50	0.75	25	20	20	5	3	0.15	0.14 (0.02-0.27)
6*	1515	20	50	0.75	25	20	20	5	3	0.25	0.14 (0.02-0.28)
7	3242	20	40	0.75	40	20	20	8	6	0.40	0.15 (0.01-0.30)
8	3442	10	50	0.75	25	20	20	5	3	0.25	0.11 (-0.02-0.25)
9	6201	20	40	1.00	50	20	20	10	6	0.50	0.15 (0.00-0.33)
10	17053	15	40	1.00	100	20	20	12	7	0.60	0.16 (-0.01-0.38)

*Presented in main part of study.

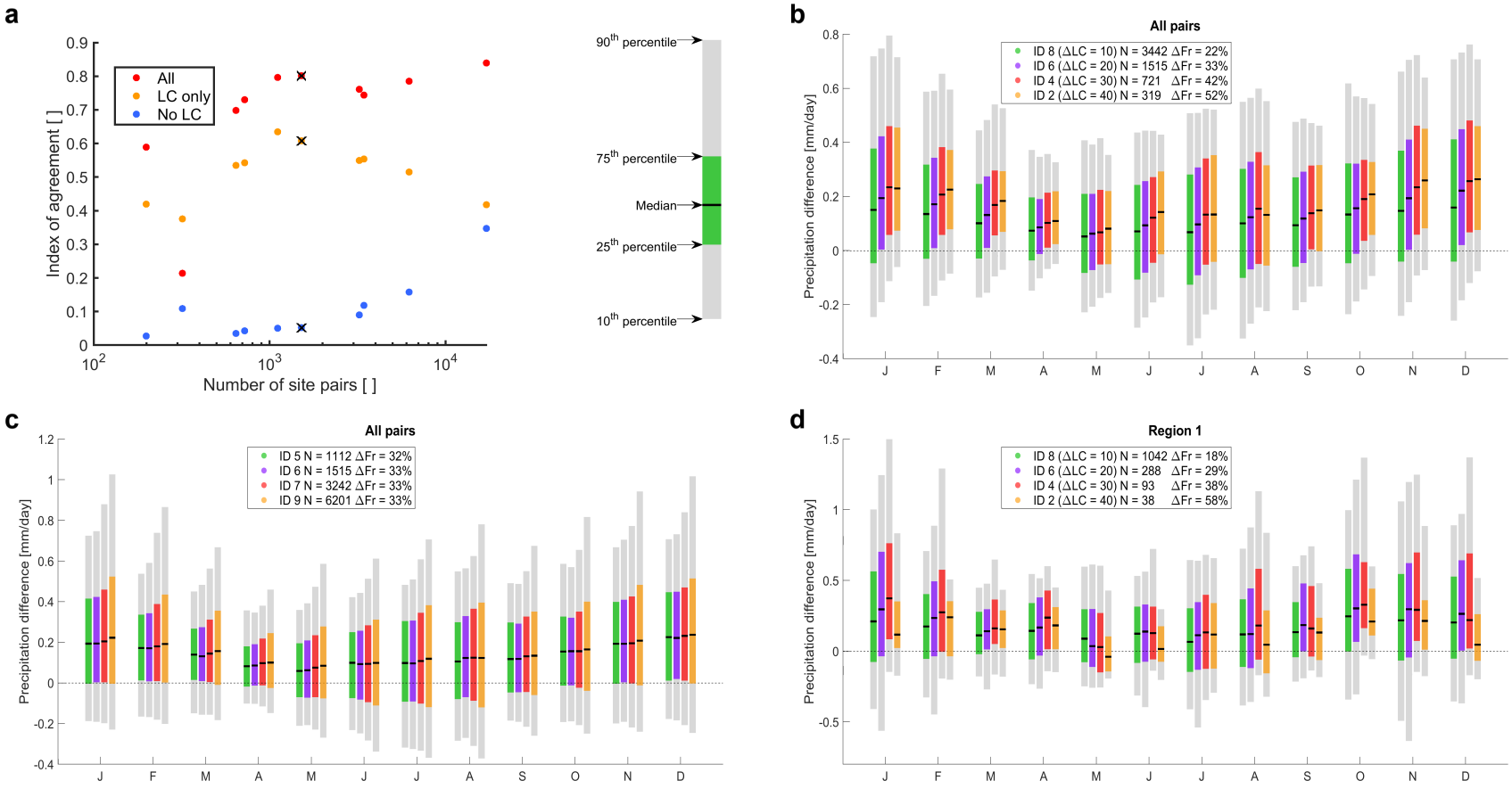

Figure D1. Panel a, IA for the different selection criteria in Table D1 between monthly median ΔP_{loc} over the five regions in Fig. 1 a of rain gauge pairs and the full GAM (red), the contribution from the difference in forest and AL_r (orange), and 'no LC' GAM (blue). Points marked with a black cross correspond to site pair analysis presented in the main part of this study. X-axis is the number of site pairs found with the respective selection criteria on a logarithmic scale. Panel b, distribution of ΔP_{loc} among rain gauge site pairs for different thresholds of the minimum difference in the fractions of AL_r and forest. Panel c, distribution of ΔP_{loc} among rain gauge site pairs with different thresholds for selection criteria other than the minimum difference in the fractions of AL_r and forest. Panel d, as panel b but for sites in Region 1 only. N is number of site pairs and ΔFr median difference in forest/rainfed agricultural land fraction among site pairs used to estimate the contribution from those LCs in the GAM.

E Uncertainty due to choice in GAM structure

The results from the GAMs, in particular ΔP_{dw}, are sensitive to the structure of the GAM. Here we present three additional GAMs to illustrate this sensitivity, besides the GAMs presented in the main part of this study (Table E1): (1) A GAM with a more flexible pure spatial term. (2) A GAM were we removed the interaction terms of the LC-related variables with latitude and longitude, which were sometimes insignificant according to the ANOVA analysis. (3) A GAM, for which the wind-related predictor variables were calculated based on trajectories that were started 200 and 300 hPa above the surface instead of starting at the two pressure levels that produced most precipitation (but still for the same precipitation events). The 'no LC' GAM was also added in Table E1 for completeness, but is not discussed here further. To quantify the spatial autocorrelation of the residuals we compute the average Moran's I across the months for distances below 1.5° ($MI_{<1.5}$) and for distances from 1.5° to 3° ($MI_{1.5-3}$), weighting points by one divided by distance from the central point squared. For a comparison, the MSWEP precipitation fields exhibit a $MI_{<1.5}$ and $MI_{1.5-3}$ of 0.758 and 0.326, respectively.

When increasing the flexibility of the pure spatial term the resulting GAM2 represents the precipitation climatology of MSWEP better than GAM1 and reduces the spatial autocorrelation of the residuals. However, the agreement of GAM2 with the site pairs is lower than the one of GAM1, as part of ΔP_{loc} becomes incorporated in the more flexible spatial term. Looking at GAM3, it appears that its performance is weaker than GAM1 in all aspects considered. In particular, the spatial interaction terms of the LC-related variables appear relevant for the conformity of the GAMs with the site pair analysis. Nevertheless, the overall features of ΔP_{loc} are similar for the individual GAMs, indicating that this part of the precipitation signal from forestation is robust (Fig. E1). Larger discrepancies emerge for ΔP_{dw}, in particular regarding the strength of the signal in summer over the central parts of Europe (Fig. E2). Notably, the selection of the starting heights when calculating the wind trajectories has a distinct effect on the estimate of ΔP_{dw} (compare GAM1 and GAM4). GAM4 even represents the precipitation climatology of MSWEP slightly better than GAM1, even though the underlying wind trajectories are presumably less tightly linked to the precipitation events for GAM4. Based on this argument, we have decided to utilize the trajectories for which the starting heights were based on the production of precipitation to generate the results presented in the main part of this study. All things considered, the sensitivity of ΔP_{dw} on the starting heights of the wind trajectories certainly deserves further attention in future studies.

Table E1. Sensitivity tests for GAM structure. First column, ID used for respective GAM followed by changes made in comparison to GAM1, which is presented in main part of this study. Columns three to seven, adjusted R^2, root mean square error (RMSE), and index of agreement (IA) of precipitation fields simulated by GAMs in comparison to MSWEP as well as average $MI_{<1.5}$ and $MI_{1.5-3}$ of the residuals. Last column, IA of monthly median ΔP_{loc} for the five regions in Fig. 1 a between rain gauge site pairs and GAMs.

ID	Changes	R^2	RMSE	IA	$MI_{<1.5}$	$MI_{1.5-3}$	IA_{PS}
GAM1	- (GAM presented in main part)	0.933	0.298	0.964	0.430	-0.0284	0.802
GAM2	k=20, sp=3 for pure spatial term instead of 15 and 5	0.942	0.279	0.969	0.407	-0.0170	0.769
GAM3	no 'prox_LC_i, lat, lon' and 'uw_pct_LC_i, lat, lon' terms	0.930	0.303	0.963	0.434	-0.0288	0.749
GAM4	Trajectories starting from 200 and 300 hPa above surface	0.936	0.293	0.966	0.417	-0.0249	- (0.80)*
no LC	Terms including prox_LC_i removed	0.921	0.319	0.957	0.448	-0.0286	0.0910

* Not directly comparable as different trajectories affects uw_pct_opwa and uw_cd criteria in site pair selection.

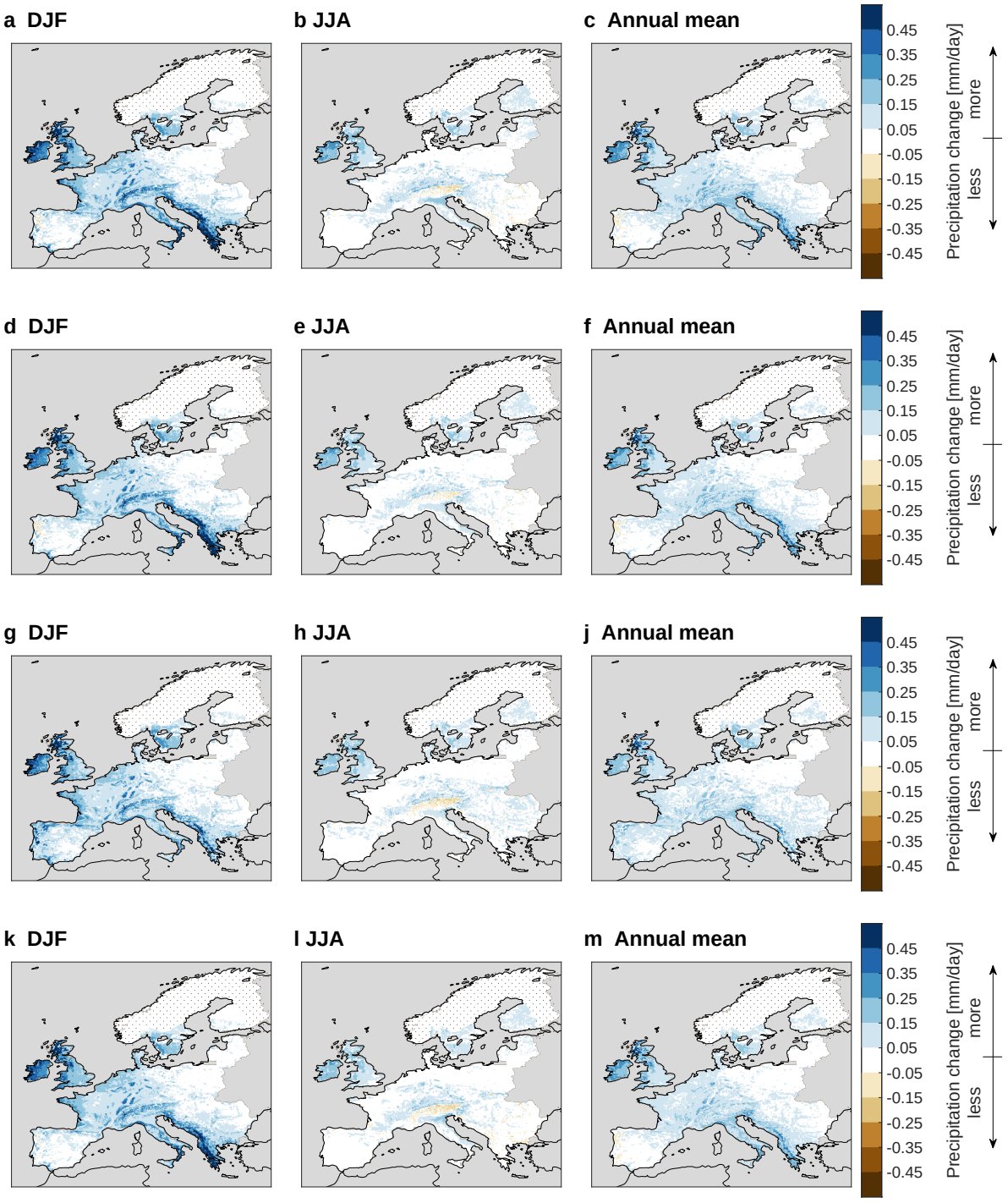

Figure E1. Estimated ΔP_{loc} from foresting 20 % of the land surface according to GAM1 (a-c, Fig. 2 a-c repeated for convenience), GAM2 (d-f), GAM3 (g-j), and GAM4 (k-m) in Table E1. Left column boreal winter, middle column boreal summer, and right column annual mean.

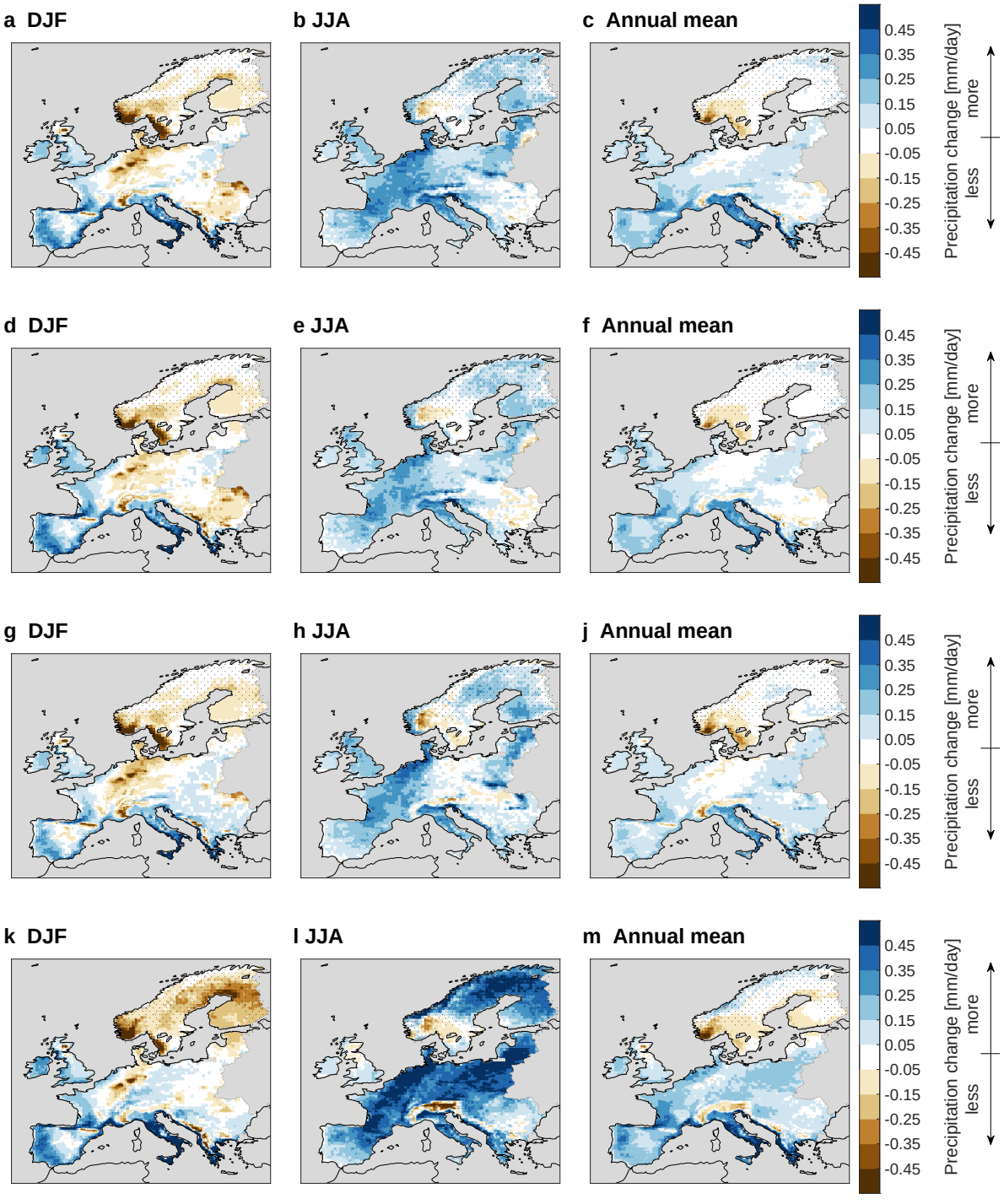

Figure E2. As Fig. E1 but for ΔP_{dw}.

F Supplementary figures and tables

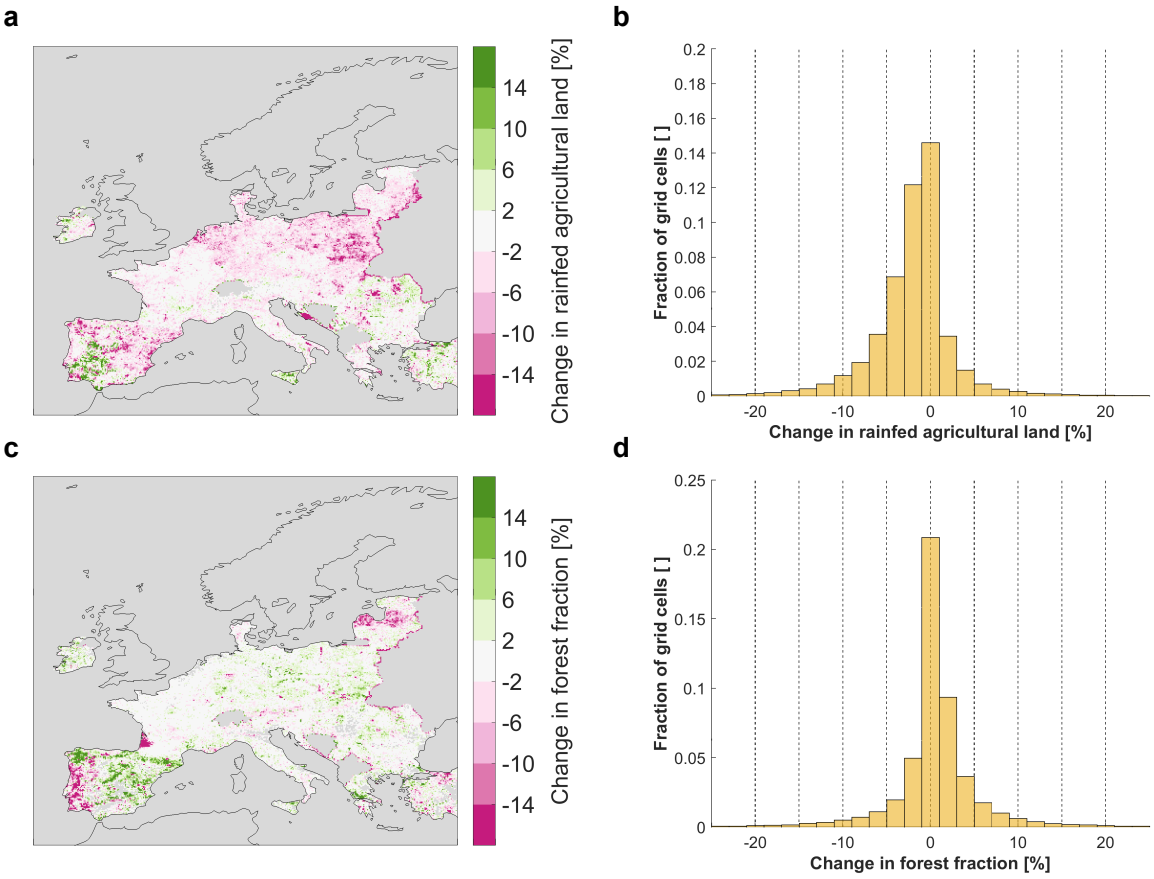

Supplementary Figure 1. Changes in AL_r and forest between 1990 and 2018. Panel a, spatial map of change in AL_r fraction according to CLC and panel b histogram of these changes. Panels c and d, the same for the forest fraction. Note that fewer countries were included in CLC of 1990 resulting in missing data for some areas.

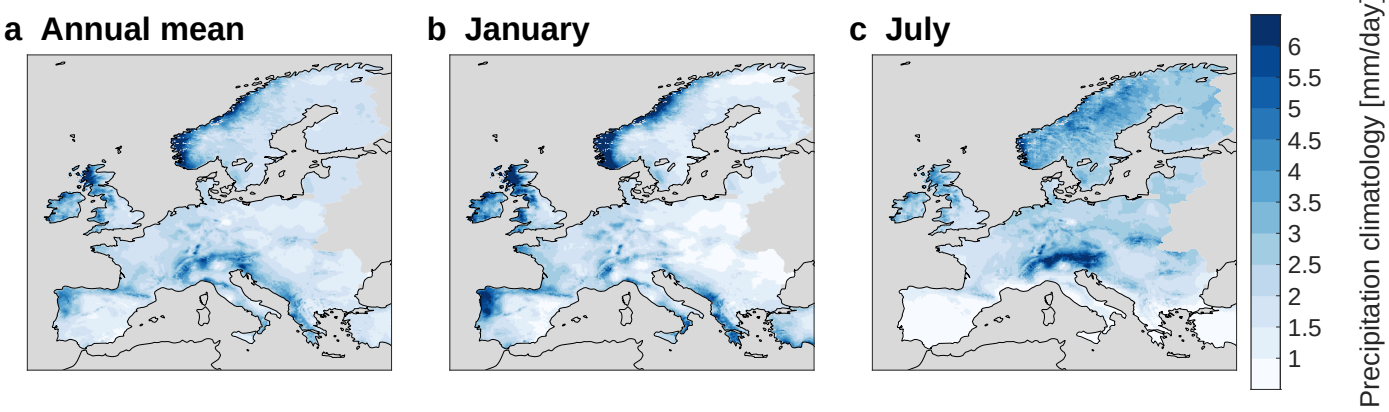

Supplementary Figure 2. Climatology in daily precipitation of MSWEP over 1986-2015 averaged over the entire year (a), January (b), and July (c).

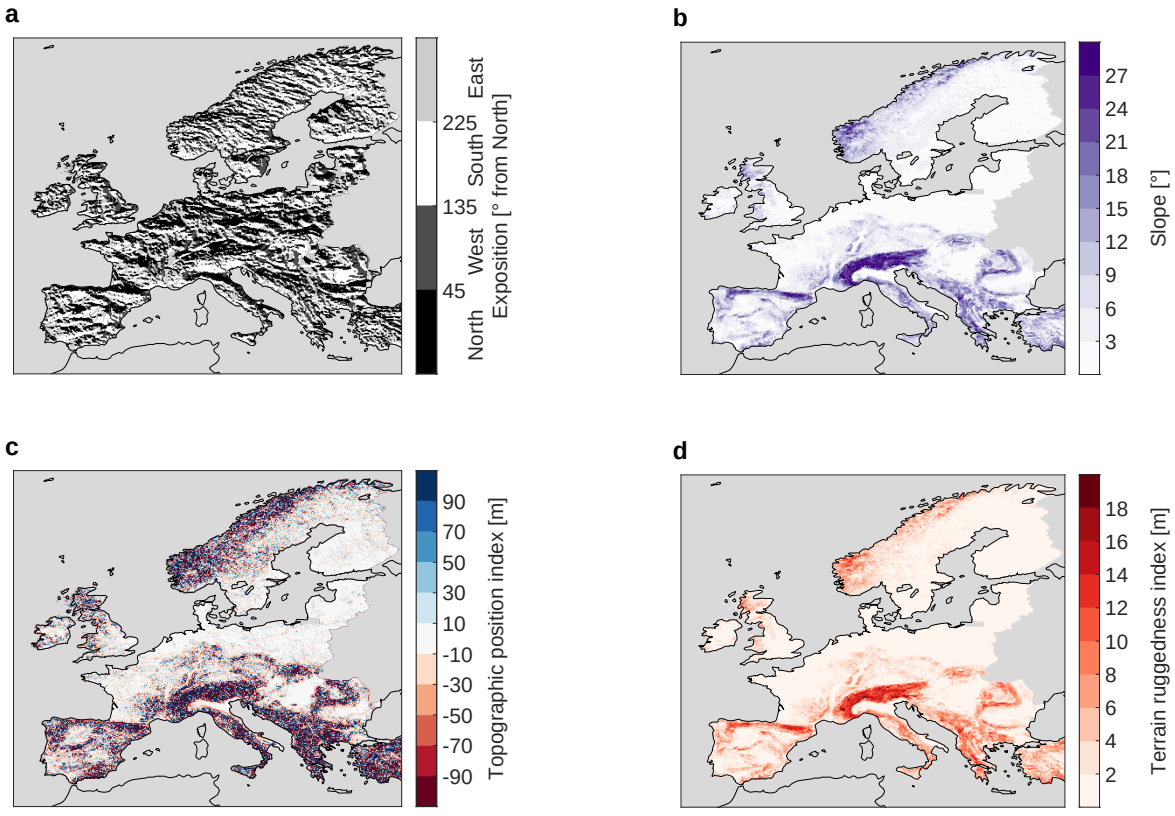

Supplementary Figure 3. Exposition (a), slope (b), topographic position index (c), and terrain ruggedness index (d) based on EU-DEM.

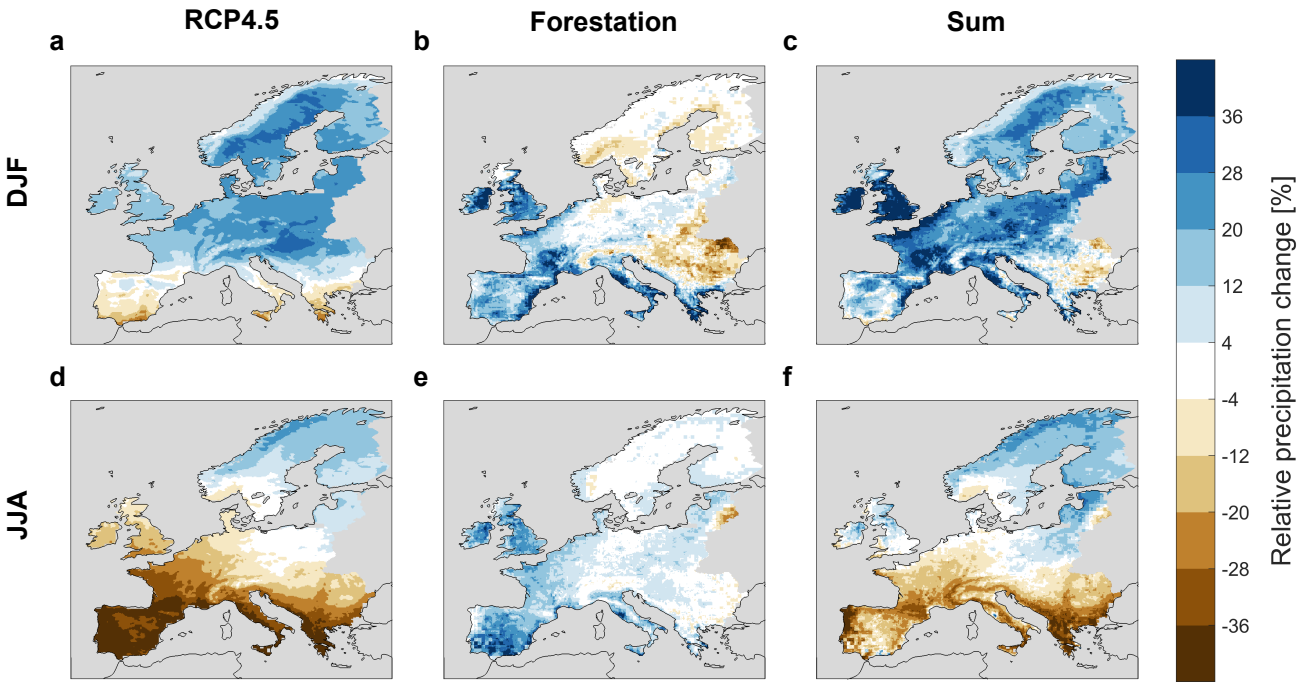

Supplementary Figure 4. As Fig. 4 but for RCP8.5.

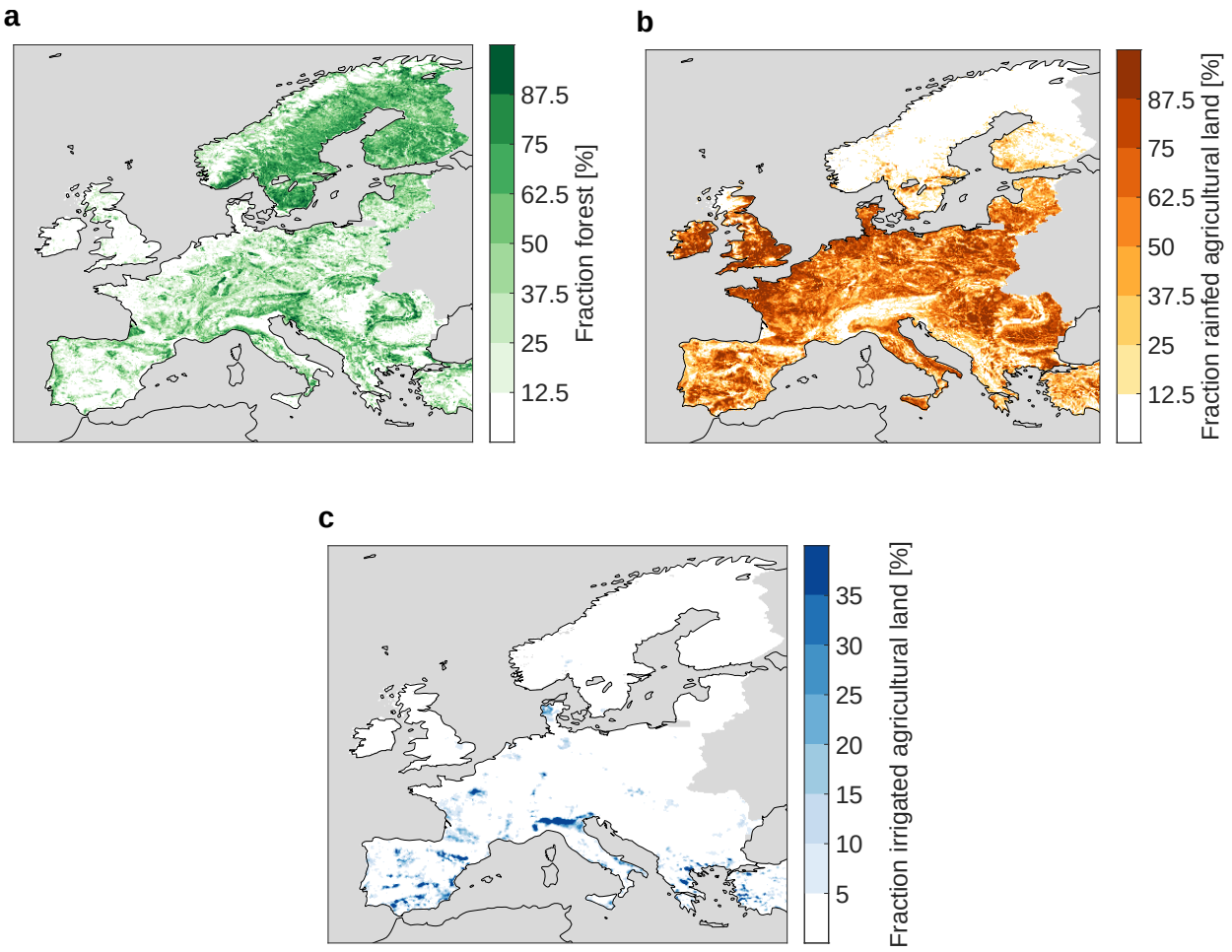

Supplementary Figure 5. Fraction of land covered by forest (a), AL_r (b), and irrigated agricultural land (c).

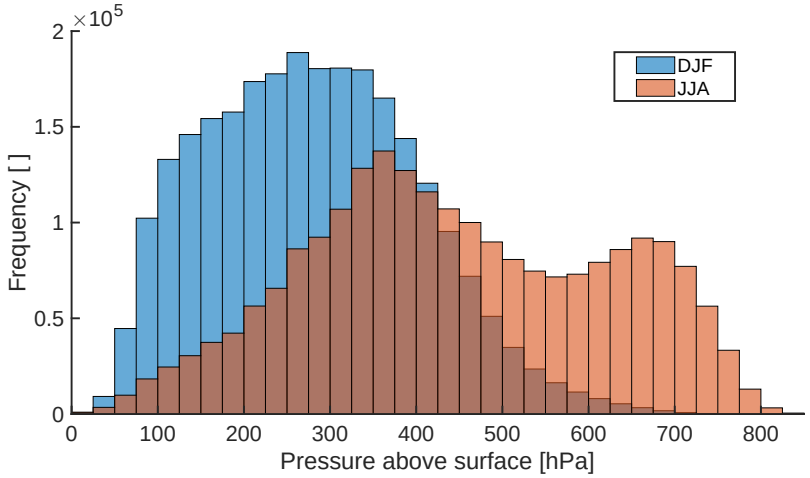

Supplementary Figure 6. Histogram of the two vertical levels in ERA5 reanalysis data that produced most precipitation. Blue bars boreal winter (DJF) and red bars boreal summer (JJA). X-axis is pressure above the surface pressure.

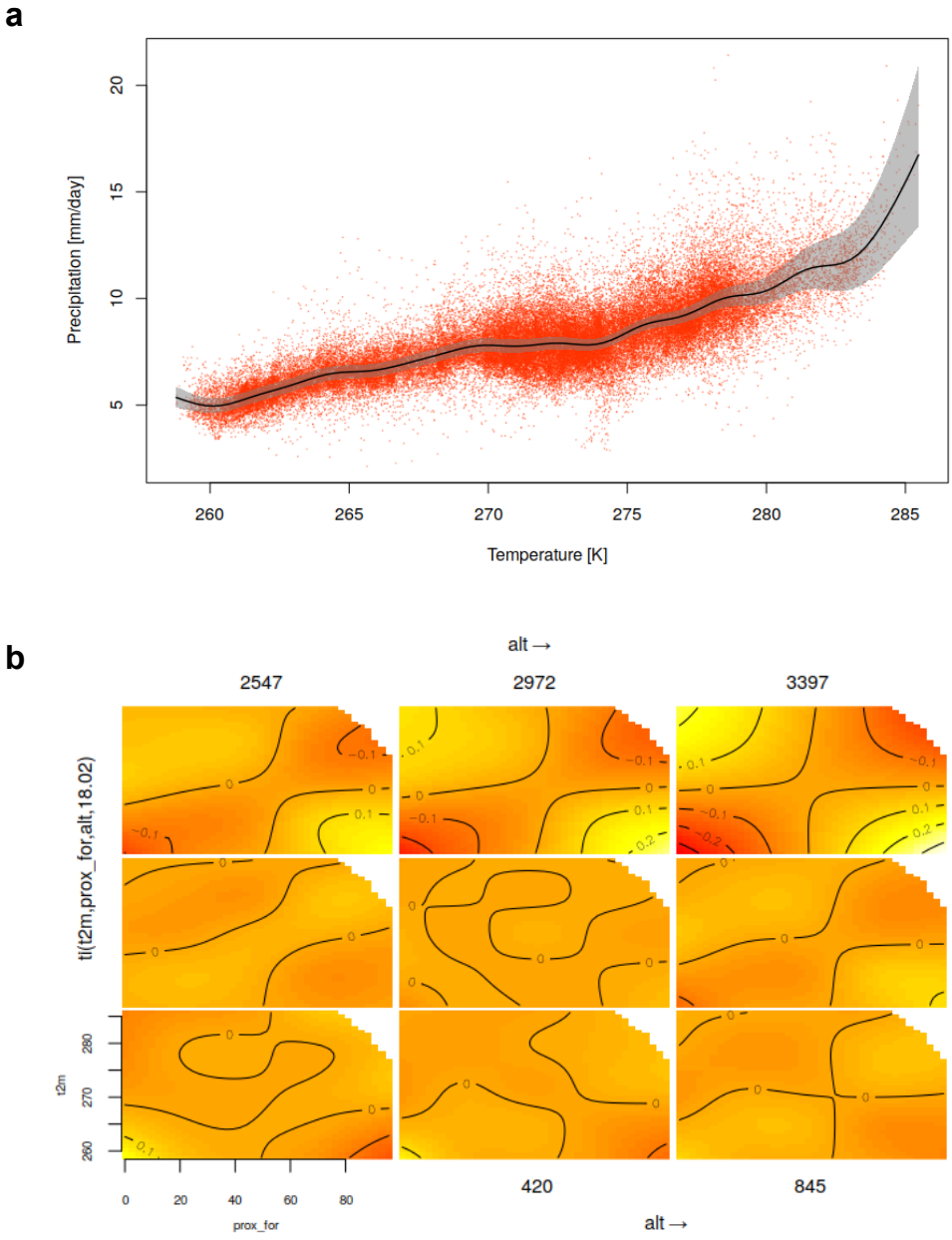

Supplementary Figure 7. Example of smooth functions. Panel a, thin plate regression spline ('s' smooth) of 2 m temperature in January (black) with standard error (grey) and partial residuals (orange). Panel b, tensor product smooth ('ti' smooth) for the proximity forest, 2 m temperature, and altitude term in January. Each panel shows a two dimensional smooth for proximity forest (X-axis) and 2 m temperature (Y-axis) at a specific altitude. Contours are the precipitation smooth. Note that a smooth of variables that are present in several other smooths cannot be interpreted in isolation.

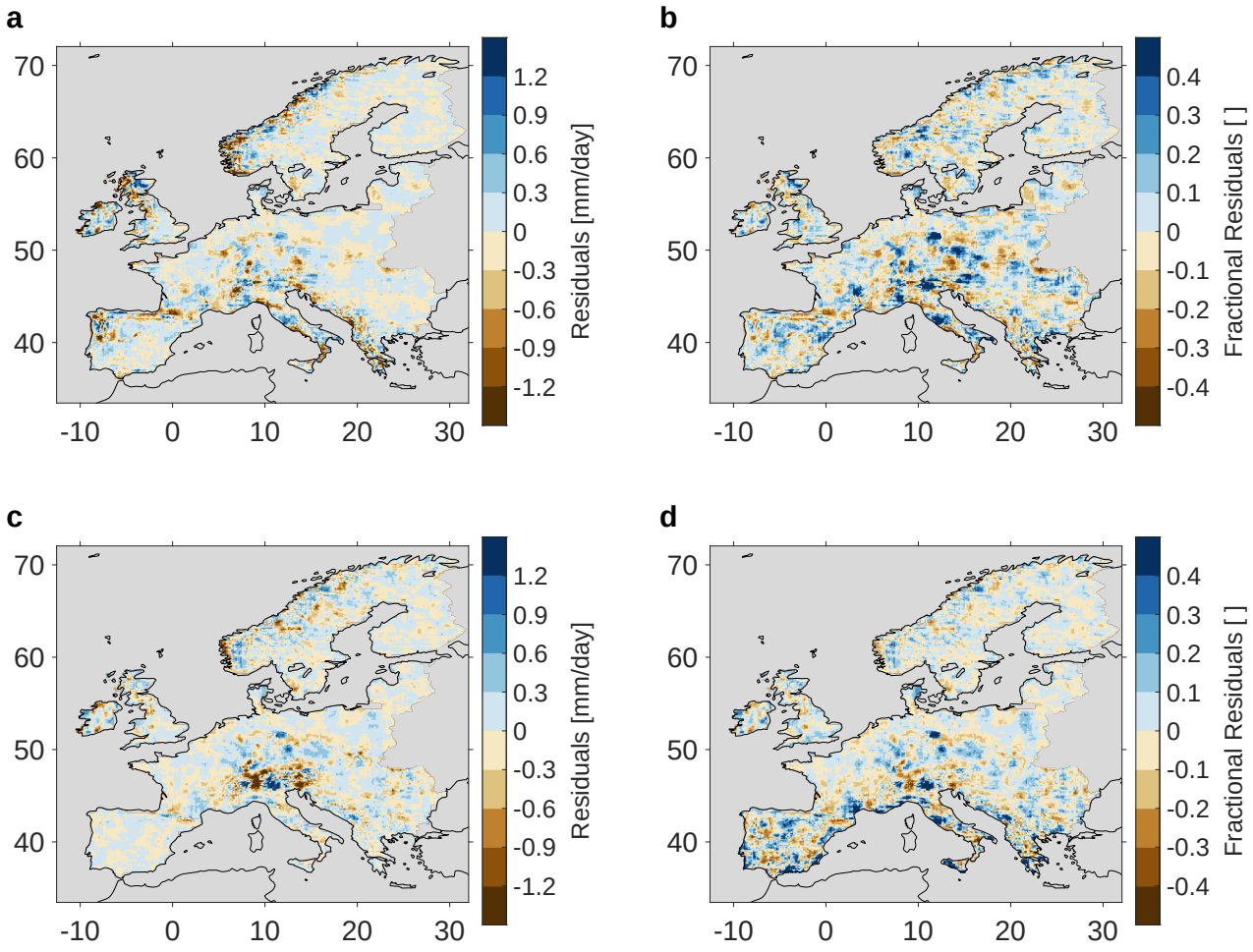

Supplementary Figure 8. Residuals of GAM-modeled precipitation fields in January (a) and July (c). To the right the residuals as a fraction of the precipitation climatology in MSWEP in January (b) and July (d).

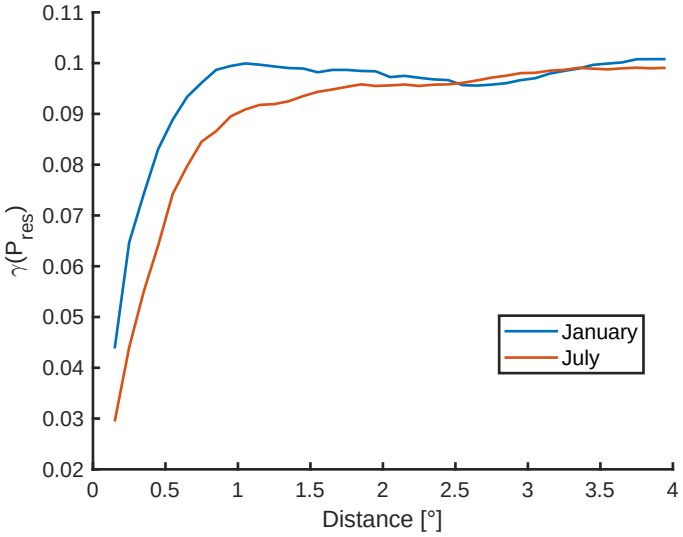

Supplementary Figure 9. Area-weighted semivariogram of the GAM residuals in January (blue) and July (orange).

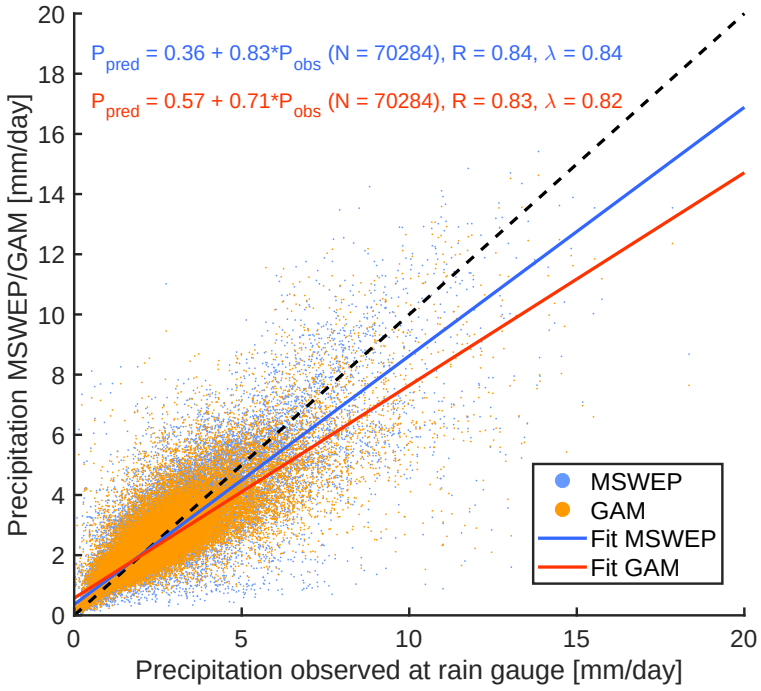

Supplementary Figure 10. Comparison of monthly precipitation climatologies between the rain gauge data and original MSWEP precipitation climatology at the respective locations (blue dots) and the GAM fit of MSWEP (orange dots). Black, blue, and red lines show the 1:1 line, a linear fit of the original MSWEP data, and a linear fit of the GAM data, respectively. On top is shown the formula of the linear fit, the Pearson correlation coefficient, and the IA.

Supplementary Table 1. As Table. 1 but for RCP8.5 (fields displayed in Supplementary Fig. 4).

ΔP ± MAD [%]	DJF			JJA		
Region	RCP 8.5	Forestation	Sum	RCP 8.5	Forestation	Sum
Mediterranean	-4.8 ± 7.1	23 ± 9.7	18 ± 12	-39 ± 3.9	19 ± 8.9	-21 ± 9.1
Atlantic	14 ± 4.8	16 ± 11	31 ± 12	-19 ± 10	14 ± 5.6	-4.7 ± 11
Alpine	14 ± 8.1	-0.79 ± 4.2	13 ± 8.0	0.75 ± 17	1.7 ± 2.5	2.4 ± 18
Continental	19 ± 6.4	-1.0 ± 9.3	18 ± 12	-13 ± 9.2	4.8 ± 3.6	-7.7 ± 9.8
Boreal	23 ± 3.3	-2.1 ± 4.1	21 ± 5.2	9.3 ± 4.8	2.9 ± 3.3	12 ± 6.5

Supplementary Table 2. Overview of the different data sets and softwares used in this study, the variables derived from them, their reference, and their availability.

Date set	Variables	Reference	Data availability
GSDR	In-situ precipitation	Lewis et al. (2019)[5]	Upon request from Elizabeth Lewis
GHCN-Daily v3.20	In-situ precipitation	Menne et al. (2012)[6,7]	ftp://ftp.ncdc.noaa.gov/pub/data/ghcn/daily/
MSWEP v2.2	Gridded precipitation	Beck et al. (2019)[8]	https://platform.princetonclimate.com/PCA_Platform/
EU-DEM v1.1	alt, slope, expo, TPI, TRI	EEA (2014)[9]	https://land.copernicus.eu/imagery-in-situ/eu-dem/eu-dem-v1.1
CLC	pct_LC$_i$, prox_LC$_i$, uw_pct_LC$_i$	Kosztra et al. (2019)[10]	https://land.copernicus.eu/pan-european/corine-land-cover/clc-2000
GMIA5	pct$_{agr_irr}$, prox$_{agr_irr}$, uw_pct$_{agr_irr}$	Siebert et al. (2013)[11]	http://www.fao.org/aquastat/en/geospatial-information/global-maps-irrigated-areas
ERA5	uw_hd, dw_hd, uw_cd, uw_pct_LC$_i$, uw_ct	C3S (2017)[12]	https://cds.climate.copernicus.eu
ERA5-Land	t2m	C3S (2019)[2]	https://cds.climate.copernicus.eu
WRPM	Reforestation potential	Griscom et al. (2017)[13,14]	https://zenodo.org/record/883444
CH2018	Climate change signal	National Centre for Climate Services[15]	https://doi.org/10.18751/climate/scenarios/ch2018/1.0
Software	**Variables**	**Reference**	**Data availability**
GDAL	alt, slope, expo, TPI, TRI	-	https://cran.r-project.org/web/packages/rgdal/index.html
LAGRANTO	uw_hd, dw_hd, uw_cd, uw_pct_LC$_i$, uw_ct	Wernli and Davies (1997)[16], Sprenger and Wernli (2015)[17]	www.lagranto.ethz.ch
mgcv	Estimated precipitation changes	Wood (2011)[18], Wood (2017)[19]	https://cran.r-project.org/web/packages/mgcv/index.html

Supplementary Table 3. List of abbreviations used in this study.

	Abbreviation	Long name/description
Variables	alt	Altitude [m]
	dw_hd	Downwind height difference [m]
	expo	Exposition [° from North]
	pct_LC$_i$	Fraction of land cover *i* [%]
	prox_LC$_i$	Proximity fraction of land cover *i* [%]
	TPI	Topographic position index [m]
	TRI	Terrain ruggedness index [m]
	t2m	2 m air temperature [K]
	uw_cd	Upwind distance to coast [° from coast]
	uw_ct	Upwind time to coast [h]
	uw_hd	Upwind height difference [m]
	uw_pct_LC$_i$	Upwind fraction of land cover *i* [%]
	PS	Propagation speed of wind trajectories [m/s]
	WS	Wind speed 10 m above surface [m/s]
Datasets	CLC	CORINE Land Cover 2000
	GSDR	Global Sub-Daily Rainfall Dataset
	GHCN	Global Historical Climatology Network
	GMIA5	Global Map of Irrigation Areas version 5
	MSWEP	Multi-Source Weighted-Ensemble Precipitation version 2.2
	WRPM	World Reforestation Potential Map
Other	AL$_r$	Rainfed agricultural land
	fREML	Fast restricted maximum likelihood method
	GAM	Generalized additive model
	GDAL	Geospatial Data Abstraction software Library 2019
	IA	Index of agreement
	k	Maximum number of nodes (in a smooth/spline)
	LC	Land cover
	LCC	Land cover change
	mgcv	Mixed GAM Computation Vehicle with Automatic Smoothness Estimation
	s	Thin plate regression spline
	sp	Smoothing parameter
	ti	Tensor product smooth
	ΔP_{dw}	Downwind change in precipitation due to forestation
	ΔP_{loc}	Local change in precipitation due to forestation, local precipitation difference of sites with more forest minus site with more AL$_r$

Supplementary Table 4. Aggregation of the CLC classes (https://land.copernicus.eu/user-corner/technical-library/corine-land-cover-nomenclature-guidelines/html) to the LC types used in this study. Left column the names of the classes used in this study, middle column CLC classes aggregated to respective class, and right column fraction of study domain covered by respective class.

Name	CLC classes	Fraction [%]
Artificial surfaces	1. Artificial Surfaces (classes 1-11)	3.7
Rainfed agricultural land	2. Agricultural areas (classes 12-22)[a]	39.2
Irrigated agricultural land	2. Agricultural areas (classes 12-22)[b]	1.8
Forest	3.1 Forest (classes 23-25)	32.7
Natural low vegetation	3.2.1 Natural grassland and 3.2.2 Moors and heathland (classes 26-27)	5.3
Shrubland	3.2.3 Sclerophyllous vegetation and 3.2.4 Transitional woodland/shrub (classes 28-29)	6.9
Natural bare land	3.3 Open spaces with little or no vegetation (classes 30-34)	4.0
Wetland	4. Wetlands (35-39)	2.7
Open water	5. Water bodies (classes 40-44)	3.9

[a] "2. Agricultural areas" in CLC minus irrigated agricultural land.

[b] Minimum of irrigated agricultural land fraction according to Global Map of Irrigated Areas version 5 and "2. Agricultural areas" in CLC.

Supplementary Table 5. Ensemble of EUR-11 regional climate model (RCM) simulations forced by RCP4.5 and RCP8.5 in CH2018. Middle column name of driving general circulation model (GCM) and right column number of ensemble members.

RCM Name	Driving GCM	N
CLMcom-CCLM4-8-17	ICHEC-EC-EARTH	1
CLMcom-CCLM4-8-17	MOHC-HadGEM2-ES	1
CLMcom-CCLM4-8-17	MPI-M-MPI-ESM-LR	1
DMI-HIRHAM5	ICHEC-EC-EARTH	1
MPI-CSC-REMO2009	MPI-M-MPI-ESM-LR	2
SMHI-RCA4	ICHEC-EC-EARTH	1
SMHI-RCA4	IPSL-IPSL-CM5A-MR	1
SMHI-RCA4	MOHC-HadGEM2-ES	1
SMHI-RCA4	MPI-M-MPI-ESM-LR	1

References

1. Van der Ent, R. J. & Savenije, H. H. G. Length and time scales of atmospheric moisture recycling. *Atmospheric Chem. Phys.* **11**, 1853–1863, DOI: 10.5194/acp-11-1853-2011 (2011).
2. Copernicus Climate Change Service (C3S). C3S ERA5-Land reanalysis (2019).
3. Sodemann, H., Schwierz, C. & Wernli, H. Interannual variability of greenland winter precipitation sources: Lagrangian moisture diagnostic and north atlantic oscillation influence. *J. Geophys. Res.-Atmos.* **113**, DOI: 10.1029/2007JD008503 (2008). https://agupubs.onlinelibrary.wiley.com/doi/pdf/10.1029/2007JD008503.
4. Aemisegger, F. *et al.* Deuterium excess as a proxy for continental moisture recycling and plant transpiration. *Atmos. Chem. Phys.* **14**, 4029–4054, DOI: 10.5194/acp-14-4029-2014 (2014).
5. Lewis, E. *et al.* GSDR: A global sub-daily rainfall dataset. *J. Clim.* **32**, 4715–4729, DOI: 10.1175/JCLI-D-18-0143.1 (2019). https://doi.org/10.1175/JCLI-D-18-0143.1.
6. Menne, M. J., Durre, I., Vose, R. S., Gleason, B. E. & Houston, T. G. An overview of the global historical climatology network-daily database. *J. Atmospheric Ocean. Technol.* **29**, 897–910, DOI: 10.1175/JTECH-D-11-00103.1 (2012). https://doi.org/10.1175/JTECH-D-11-00103.1.
7. Menne, M. J. *et al.* Global Historical Climatology Network - Daily (GHCN-Daily), Version 3.20, DOI: 10.7289/V5D21VHZ (2012).
8. Beck, H. E. *et al.* MSWEP V2 global 3-hourly 0.1° precipitation: Methodology and quantitative assessment. *B. Am. Meteorol. Soc.* **100**, 473–500, DOI: 10.1175/BAMS-D-17-0138.1 (2019).
9. EEA. EU-DEM statistical validation (2014).
10. Kosztra, B., Büttner, G., Hazeu, G. & Arnold, S. Updated CLC illustrated nomenclature guidelines (2019).
11. Siebert, S., Henrich, V., Frenken, K. & Burke, J. *Global Map of Irrigation Areas version 5*. Rheinische Friedrich-Wilhelms-University, Bonn, Germany / Food and Agriculture Organization of the United Nations, Rome, Italy (2013).
12. Copernicus Climate Change Service (C3S). ERA5: Fifth generation of ECMWF atmospheric reanalyses of the global climate (2017).
13. Griscom, B. W. *et al.* Natural climate solutions. *P. Natl. Acad. Sci. USA* **114**, 11645–11650, DOI: 10.1073/pnas.1710465114 (2017). https://www.pnas.org/content/114/44/11645.full.pdf.
14. Griscom, B. W. *et al.* Global reforestation potential map, DOI: 10.5281/zenodo.883444 (2017).
15. CH2018. 2018 Climate scenarios for Switzerland. Tech. Rep., National Centre for Climate Services (2018).
16. Wernli, B. H. & Davies, H. C. A lagrangian-based analysis of extratropical cyclones. I: The method and some applications. *Q. J. Roy. Meteor. Soc.* **123**, 467–489, DOI: 10.1002/qj.49712353811 (1997). https://rmets.onlinelibrary.wiley.com/doi/pdf/10.1002/qj.49712353811.
17. Sprenger, M. & Wernli, H. The LAGRANTO Lagrangian analysis tool - version 2.0. *Geosci. Model. Dev.* **8**, 2569–2586, DOI: 10.5194/gmd-8-2569-2015 (2015).
18. Wood, S. N. Fast stable restricted maximum likelihood and marginal likelihood estimation of semiparametric generalized linear models. *J. R. Stat. Soc.* **73**, 3–36, DOI: 10.1111/j.1467-9868.2010.00749.x (2011). https://rss.onlinelibrary.wiley.com/doi/pdf/10.1111/j.1467-9868.2010.00749.x.
19. Wood, S. N. *Generalized additive models : an introduction with R*. Chapman & Hall/CRC texts in statistical science (CRC Press/Taylor & Francis Group, Boca Raton, 2017), second edition edn.